

APPENDIX

Text A1. Data quality justification

The linear regression between $\delta^{29}\text{Si}$ and $\delta^{30}\text{Si}$ of $\text{Si}(\text{OH})_4$ samples, either with or without brucite coprecipitation, is very close to the mass-dependent equilibrium or kinetic fractionation line (Fig. A1), indicating determination of $\delta^{30}\text{Si}$ free of polyatomic interferences. In addition, the old (November 2013 and February 2012, some without brucite coprecipitation; Table A1) and new (May 2018, all with brucite coprecipitation; Table 1) data collected in the ARE show a good linear relationship between $\delta^{30}\text{Si}_{\text{Si}(\text{OH})_4}$ and $\ln(\text{Si}(\text{OH})_4)$ (Fig. A5), which suggests that both datasets are intrinsically comparable despite different pre-treatments.

Text A2. Another cruise to the Amazon River Estuary

Sampling and analyses

In the ARE, a single upstream station at zero salinity was sampled in November 2013 and other stations on the shelf were investigated during R/V *Maria S. Merian* cruise MSM20-3 (Mulitza et al., 2013) in February 2012 (Fig. A2), during which the monthly discharges were $3.2 \times 10^{11} \text{ m}^3$ and $5.1 \times 10^{11} \text{ m}^3$, respectively (data from Óbidos observation station; <http://www.orehybam.org>). Water samples for Si(OH)_4 concentration and $\delta^{30}\text{Si}_{\text{Si(OH)}_4}$ analyses were taken from the ship's centrifugal pump, which has an inlet system at 6.5 m water depth. About 200 ml of each sample was subsequently filtered using a system consisting of a polysulfide holder connected to a water jet pump and a polycarbonate membrane filter (0.4 μm pore size and 47 mm diameter) and ~100 ml out of these were transferred to acid-cleaned polyethylene bottles. After filtering, the samples were acidified with 0.1 ml concentrated ultrapure HNO_3 .

Salinities of surface water samples were determined with the ship's thermosalinograph system (SBE45 MicroTSG, Sea-Bird). Si(OH)_4 concentrations in the water samples were analyzed following classical colorimetric methods, using a traditional spectrophotometer. For $\delta^{30}\text{Si}_{\text{Si(OH)}_4}$ measurements, Si(OH)_4 with low Si(OH)_4 concentrations ($<39 \mu\text{mol L}^{-1}$; Table A1) was pre-concentrated and separated from the major matrix elements using a two-step brucite coprecipitation technique (Reynolds et al., 2006), which was further purified using cation-exchange chromatography (Georg et al., 2006). Other high Si(OH)_4 concentration samples ($>39 \mu\text{mol L}^{-1}$; Table A1) were directly purified using cation-exchange chromatography given that their Si(OH)_4 content is high enough to produce detectable signals on the MC-ICP-MS.

Biological fractionation during diatom growth

In February 2012, surface Si(OH)_4 concentrations generally decreased from the upper estuaries to the shelf (Fig. A3b) reflecting high riverine input of nutrients to the coastal shelf areas. Si(OH)_4 concentrations ($3.7\text{--}125.3 \mu\text{mol L}^{-1}$) were overall comparable to or slightly lower than those in May 2018 ($0.6\text{--}150.2 \mu\text{mol L}^{-1}$) (Fig. A3e). $\delta^{30}\text{Si}_{\text{Si(OH)}_4}$ signatures were significantly heavier in surface seawaters than in the river waters in February 2012 (2.6 vs. 1.3‰; Fig. A3c; Table A1), which is similar to the $\delta^{30}\text{Si}_{\text{Si(OH)}_4}$ distribution in May 2018 (3.0 vs. 1.2‰; Fig. A3f; Table 1).

We also used the two-endmember mixing model and Si isotope fractionation model to estimate the isotopic enrichment factor $^{30}\epsilon$ in the surface waters of the ARE in February 2012 (Fig. A4). Salinity, Si(OH)_4 concentration, and $\delta^{30}\text{Si}_{\text{Si(OH)}_4}$ values for the river water endmember are applied based on the field measurements either at the river station in November 2013 (0.0, $125.3 \mu\text{mol L}^{-1}$, and $1.3 \pm 0.2\text{‰}$, respectively) or at station M147_66-1 in May 2018 (0.0, $150.2 \mu\text{mol L}^{-1}$, and $1.2 \pm 0.2\text{‰}$, respectively). The corresponding data for the seawater endmember are 35.6, $3.7 \mu\text{mol L}^{-1}$, and $2.6 \pm 0.2\text{‰}$, respectively, based on the field measurements at station B01x in February 2012 (Table A1).

Independent of the selected river water endmembers, significant removal of Si(OH)_4 corresponding to elevated $\delta^{30}\text{Si}_{\text{Si(OH)}_4}$ was revealed at mid- and high salinities of 15.5–29.1 (Fig. A4a, b), reflecting preferential utilization of Si(OH)_4 with lighter Si isotopic composition. The average isotopic enrichment factor $^{30}\epsilon$ was estimated to be $-1.0 \pm 0.4\text{‰}$ (Rayleigh model) or $-1.4 \pm 0.5\text{‰}$ (steady state model) based on the river water endmember in November 2013, with Si(OH)_4 consumption of $47 \pm 2\%$ (calculated as $1-f$; Eqs. 2 and A3). The average isotopic enrichment factor $^{30}\epsilon$ was estimated to be $-1.0 \pm 0.3\text{‰}$ (Rayleigh model) or $-1.4 \pm 0.4\text{‰}$ (steady state model) based on the river water endmember in May 2018, with Si(OH)_4 consumption of $55 \pm 1\%$.

(calculated as $1-f$; Eqs. 2 and A3). The $^{30}\epsilon$ values are all consistent with those estimated from the new ARE dataset collected in May 2018 (Fig. A4c, d), which are $-1.0 \pm 0.4\text{‰}$ (Rayleigh model) or $-1.6 \pm 0.4\text{‰}$ (steady state model). A previous study has shown that the largest Si(OH)_4 depletion during diatom bloom is frequently observed on the shelf off the ARE in March (DeMaster et al., 1996). Data obtained during the AmasSeds program also showed the highest bSi production rates at the Amazon shelf break in March (Shipe et al., 2006), which is very close to the sampling season of the data presented here (February; Mulitza et al., 2013).

Text A3. Two-endmember mixing model

The conservative two-endmember mixing of Si isotopes between river water and seawater in estuaries can be predicted by the following equations:

$$F_{e1} + F_{e2} = 1 \quad (A1)$$

$$Salinity_{con} = Salinity_{e1} \times F_{e1} + Salinity_{e2} \times F_{e2} \quad (A2)$$

$$[Si(OH)_4]_{con} = [Si(OH)_4]_{e1} \times F_{e1} + [Si(OH)_4]_{e2} \times F_{e2} \quad (A3)$$

$$\delta^{30}Si_{Si(OH)_4_{con}} = \frac{\delta^{30}Si_{Si(OH)_4_{e1}} \times [Si(OH)_4]_{e1} \times F_{e1} + \delta^{30}Si_{Si(OH)_4_{e2}} \times [Si(OH)_4]_{e2} \times F_{e2}}{[Si(OH)_4]_{e1} \times F_{e1} + [Si(OH)_4]_{e2} \times F_{e2}} \quad (A4)$$

The subscripts “e1” and “e2” denote the river water endmember and the seawater endmember. “F_{e1}” and “F_{e2}” are the respective fractions of the two endmember water masses leading to the measured composition of a given water sample. The subscript “con” denotes the conservative properties of the samples exclusively resulting from the two-endmember mixing based on salinity, Si(OH)₄, and $\delta^{30}Si_{Si(OH)_4}$, which are taken as an initial condition prior to any chemical or biological alterations.

Text A4. Changing $\delta^{30}\text{Si}_{\text{Si}(\text{OH})_4}$ signatures of the Amazon river water endmember and heavier $\delta^{30}\text{Si}_{\text{Si}(\text{OH})_4}$ signature of the Yangtze river water endmember

Hughes et al. (2013) showed temporal variations of $\delta^{30}\text{Si}_{\text{Si}(\text{OH})_4}$ at Óbidos observation station in the Amazon main stream, which increased from 0.8‰ in May to 1.3‰ in October and to 1.8‰ in November 2010, corresponding to an increase in $\text{Si}(\text{OH})_4$ concentrations from 124 to 134 and to 145 $\mu\text{mol L}^{-1}$. This contrast indicates that the seasonal variability of Si dynamics is highly complex in the Amazon River drainage basin, which is controlled by multiple processes including bSi production by diatoms and higher plants, weathering, and secondary clay formation. However, the integrated $\delta^{30}\text{Si}_{\text{Si}(\text{OH})_4}$ signature exported to the estuary (weighted for $\text{Si}(\text{OH})_4$ flux) over the entire sampling period was relatively light at 0.9‰ (Hughes et al., 2013). This value is comparable to that observed previously at Óbidos observation station by De La Rocha et al. (2000), who also reported a lighter integrated value of 0.6‰ for the drainage basin of the Amazon River.

In this study, the $\delta^{30}\text{Si}_{\text{Si}(\text{OH})_4}$ signature of river water endmember was heavier in the YRE ($1.8 \pm 0.2\text{‰}$) than in the ARE ($1.2 \pm 0.2\text{‰}$) and PRE ($1.4 \pm 0.2\text{‰}$). $\delta^{30}\text{Si}_{\text{Si}(\text{OH})_4}$ in river waters, if not significantly impacted by biological $\text{Si}(\text{OH})_4$ uptake or ASi dissolution, generally reflects the weathering regime and intensity (Frings et al., 2016). In the lowland region of the Amazon basin with high weathering intensity, chemical erosion equals to total denudation. In this case, all secondary mineral phases are re-solubilized, resulting in fairly small fractionation of Si isotopes between the parent material and riverine $\text{Si}(\text{OH})_4$ (Hughes et al., 2013; Frings et al., 2016). The catchment of the Pearl River main tributary is dominated by easily erodible coarse-grained granites and poorly cemented siltstones/sandstones subject to low silicate weathering intensity (Zhang et al., 2008). We thus also predict low fractionation of Si isotopes in the Pearl River drainage basin. The Yangtze River is intermediate in the weathering intensity spectrum and shows remarkable

fractionation (Zhang et al., 2003; Frings et al., 2016), which is consistent with our observations of heavy $\delta^{30}\text{Si}_{\text{Si(OH)}_4}$ signatures of the river water endmember in the YRE.

Moreover, Ding et al. (2014) observed a progressive increase in $\delta^{30}\text{Si}_{\text{Si(OH)}_4}$ along the Yangtze River driven by the uptake of Si(OH)_4 by grasses in wetlands and rice in paddy fields due to better phytolith preservation. The increased water residence time triggered by the construction of the dam including the Three Gorges Dam also potentially leads to heavier $\delta^{30}\text{Si}_{\text{Si(OH)}_4}$ in the river due to the enhanced removal of Si(OH)_4 by either biotic or abiotic processes (Hughes et al., 2012). The Yangtze River catchment, featuring more intense chemical weathering, biological utilization, and/or anthropogenic activities than the other two river catchments, thus has an elevated $\delta^{30}\text{Si}_{\text{Si(OH)}_4}$ value of the river water endmember (i.e., $1.8 \pm 0.2\text{‰}$; Fig. 3f).

Text A5. Seawater endmember verification

The $\delta^{30}\text{Si}_{\text{Si}(\text{OH})_4}$ value of $3.2 \pm 0.3\text{‰}$ for the seawater endmember in the ARE in May 2018 is estimated based on $\text{Si}(\text{OH})_4$ concentration of the surface water at station M147_55-F and the linear relationship between $\delta^{30}\text{Si}_{\text{Si}(\text{OH})_4}$ values and $\ln(\text{Si}(\text{OH})_4)$ from all available data during the same cruise M147 (Fig. A5). The selected seawater endmembers in the YRE and the PRE are based on few field measurements and are not strict representatives of $\text{Si}(\text{OH})_4$ -depleted seawater, in particular in the PRE. We thus use previously published data of salinity, $\text{Si}(\text{OH})_4$, and $\delta^{30}\text{Si}_{\text{Si}(\text{OH})_4}$ collected in the open ocean surface waters as alternative seawater endmembers to further investigate and predict the conservative mixing of Si isotopes (Fig. A6). The data employed are those at station 69/14 in the tropical Northeast Atlantic Ocean (de Souza et al., 2012) for the ARE, at station PN03b in the East China Sea (Cao et al., 2015) for the YRE, and at stations A7, A5, A2, A10, and SEATS in the South China Sea (Cao et al., 2012) for the PRE.

In the ARE, the isotopic enrichment factor $^{30}\epsilon$ based on the seawater endmember at station 69/14 (Rayleigh model: $-1.0 \pm 0.4\text{‰}$, steady state model: $-1.6 \pm 0.4\text{‰}$; Fig. A6a) is essentially identical to that based on the seawater endmember at station M147_55-F during cruise M147 (Rayleigh model: $-1.0 \pm 0.4\text{‰}$, steady state model: $-1.6 \pm 0.4\text{‰}$; Fig. 3). In the YRE and the PRE, the data points representing the original seawater endmembers based on field measurements presented in this study (Fig. 3; Table 1) fall on the new mixing curves (Fig. A6b, c), while $\delta^{30}\text{Si}_{\text{Si}(\text{OH})_4}$ distributions still strictly fit the two-endmember mixing. As a consequence, our selection and estimation of seawater endmembers are valid.

In addition in the ARE, $^{30}\epsilon$ based on the seawater endmember at station M147_56-F (Rayleigh model: $-1.5 \pm 0.2\text{‰}$, steady state model: $-2.0 \pm 0.2\text{‰}$) is slightly larger than that based on the seawater endmember at M147_55-F. However, the low salinity (30.0) at station M147_56-F makes

130 it a sub-optimal seawater endmember during cruise M147 to the ARE.

Table A1. Salinity, dissolved silicate (Si(OH)_4) concentrations, and dissolved silicon isotopic compositions ($\delta^{30}\text{Si}_{\text{Si(OH)}_4}$) in the surface waters of the Amazon River Estuary and adjacent shelf areas in November 2013 and February 2012. “Bracketing measurement” denotes $\delta^{30}\text{Si}_{\text{Si(OH)}_4}$ analysis for a sample on a single day. “Mean” denotes the average $\delta^{30}\text{Si}_{\text{Si(OH)}_4}$ based on repeated bracketing measurements from different days. “Final reported data” present $\delta^{30}\text{Si}_{\text{Si(OH)}_4}$ of the mean except that for two samples measured once, $\delta^{30}\text{Si}_{\text{Si(OH)}_4}$ of bracketing measurement was used.

Station	Lat.	Long.	Salinity	Si(OH) ₄	Bracketing measurement		Mean	Final reported data			
					I	II					
					(°N)	(°E)	(μmol L ⁻¹)	δ ³⁰ Si _{Si(OH)₄}	δ ³⁰ Si _{Si(OH)₄}	δ ³⁰ Si _{Si(OH)₄}	δ ³⁰ Si _{Si(OH)₄}
								(‰ ± 2SD _{bracketing}) [§]	(‰ ± 2SD _{bracketing}) [§]	(‰ ± 2SD _{repeated}) [‡]	(‰ ± 2SD) [†]
November 2013											
River	0.00	−51.00	0.0	125.3	1.31 ± 0.14	1.28 ± 0.14	1.30 ± 0.04	1.30 ± 0.20			
February 2012											
B12x	1.90	−48.70	15.5	39.1	2.08 ± 0.08			2.08 ± 0.20			
B18x*	2.07	−48.75	20.3	29.9	2.22 ± 0.14	2.35 ± 0.05	2.29 ± 0.18	2.29 ± 0.20			
B20x*	2.13	−48.68	24.8	22.3	1.80 ± 0.13			1.80 ± 0.20			
B22x*	2.17	−48.65	29.1	13.2	2.05 ± 0.08	1.93 ± 0.10	1.99 ± 0.17	1.99 ± 0.20			
B01x*	1.79	−48.23	35.6	3.7	2.60 ± 0.15	2.75 ± 0.12	2.68 ± 0.21	2.68 ± 0.21			

[§] ‰ ± 2SD_{bracketing} is the average $\delta^{30}\text{Si}_{\text{Si(OH)}_4}$ together with 2 standard deviations estimated from the bracketing measurements on a single day.

[‡] ‰ ± 2SD_{repeated} is the average $\delta^{30}\text{Si}_{\text{Si(OH)}_4}$ together with 2 standard deviations estimated from the repeated bracketing measurements from different days.

[†] 2SD for the final reported data represents the long-term external reproducibility of ±0.20‰, except that for few samples with 2SD_{repeated} larger than ±0.20‰, the 2SD_{repeated} was used.

140 * Si(OH)_4 in the samples was pre-concentrated via brucite coprecipitation before cation-exchange chromatography.

141 **Table A2.** Dissolved inorganic nitrogen (DIN, nitrate plus nitrite), dissolved inorganic phosphate (DIP), total suspended matter (TSM), and
 142 chlorophyll a (Chl-a) in the surface waters of the Amazon, Yangtze, and Pearl River estuaries and adjacent shelf areas. Also included are calculated
 143 dissolved silicate ($\text{Si}(\text{OH})_4$) consumptions (1-f; Eqs. 2 and A3) and silicon isotopic enrichment factors ($^{30}\epsilon$; Eqs. 3 and 5) in the surface waters of
 144 the Amazon River Estuary.

Station	DIN ($\mu\text{mol L}^{-1}$)	DIP ($\mu\text{mol L}^{-1}$)	TSM (mg L^{-1})	Chl-a ($\mu\text{g L}^{-1}$)	Si(OH) ₄ consumption (%)	$^{30}\epsilon$ (Rayleigh model) (‰)	$^{30}\epsilon$ (steady state model) (‰)
<i>Amazon River Estuary (May 2018)</i>							
M147_66-1	12.331	0.621	ND**	1.1			
M147_70-1	14.946	0.556	ND	ND	0		
M147_69-1	15.969	0.547	ND	ND	0		
M147_71-1	12.877	0.57	ND	2.1	6		
M147_80-1	0.189	<LOD*	ND	5.8	46	-1.3	-1.7
M147-79-1	0.474	0.056	ND	5.9	35		
M147_78-1	1.722	0.07	ND	6.1	37		
M147_72-1	2.327	0.174	ND	13.5			
M147_75-1	1.051	0.109	ND	3.8	45	-1.3	-1.7
M147_74-1	0.412	<LOD	ND	7.7	51		
M147_64-1	0.348	0.097	ND	11.4	51	-0.7	-1.0
M147_56-F	<LOD	0.169	ND	0.1	94	-0.6	-1.9
M147_55-F	<LOD	0.053	ND	ND			
<i>Yangtze River Estuary (March 2015)</i>							
C4	159.3	2.64	48.7	1.08			
C5	161.3	2.43	42.7	1.16			
C6	178.8	2.76	40.3	1.51			

C7	194.1	2.91	72.0	1.82
A06-1	160.0	2.54	92.3	0.81
A06-2	105.1	2.01	103.7	1.13
A06-3	79.0	1.65	28.8	0.79
A06-4	69.1	1.50	27.0	0.75
A06-7	24.2	0.78	21.3	0.68
A06-9	12.7	0.52	23.1	1.48
A06-11	10.8	0.45	22.0	0.54

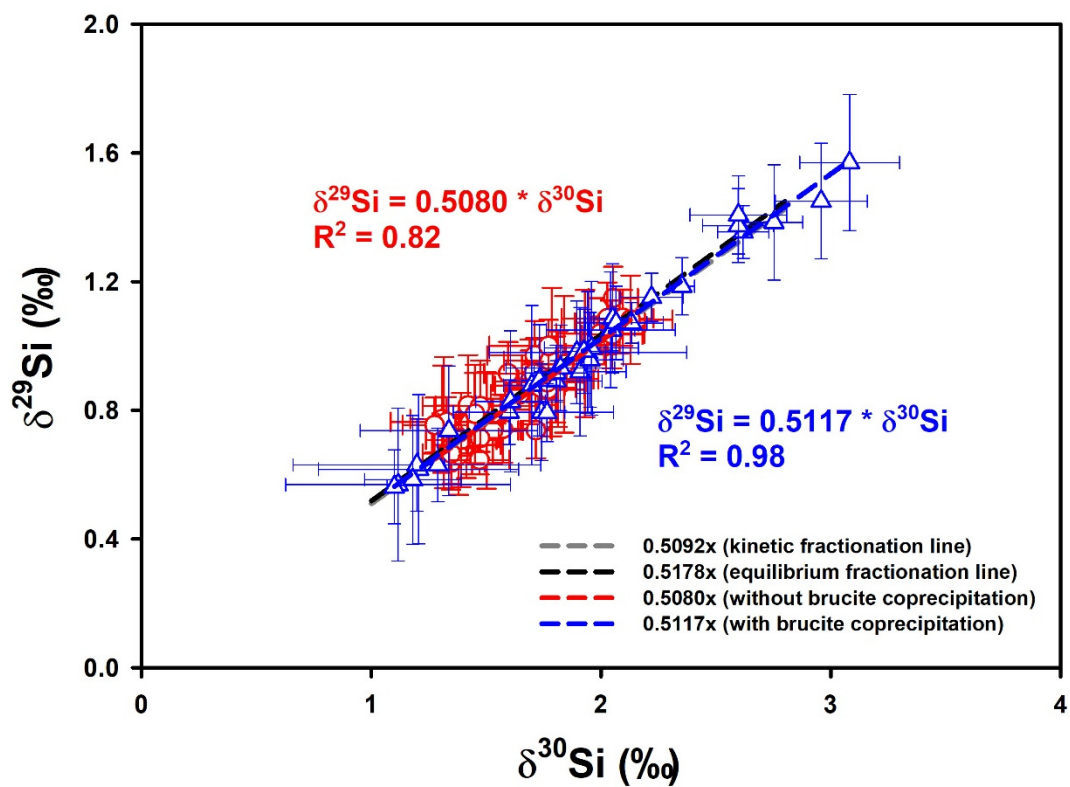
Pearl River Estuary (August 2012)

P04	197.2	2.748	26	10.63
A01	154.0	1.803	17	4.92
A02	155.0	1.753	18	6.73
A03	110.3	1.135	33	3.35
A04	103.2	1.191	33	4.90
A05	123.5	1.468	57	1.65
A06	120.1	1.431	35	1.00
A07	100.3	1.445	10	0.90
A08	70.9	1.005	5	4.81
A10	79.0	1.143	2	3.19
F406	58.2	1.097	5	1.66
F412	41.1	0.879	2	4.29
F413	37.2	0.744	3	5.36
F414	26.0	0.588	1	2.99
F415	3.9	0.327	ND	ND

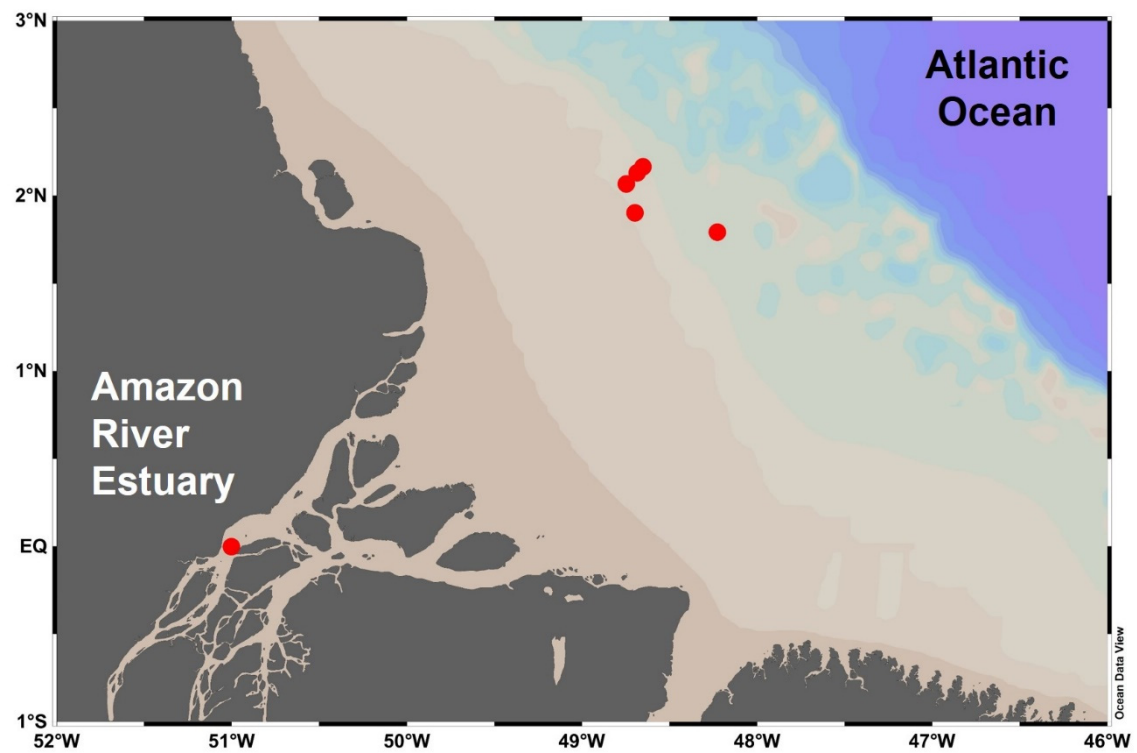
145 * <LOD means lower than the detection limit of 0.05 $\mu\text{mol L}^{-1}$.

146 ** ND means not determined.

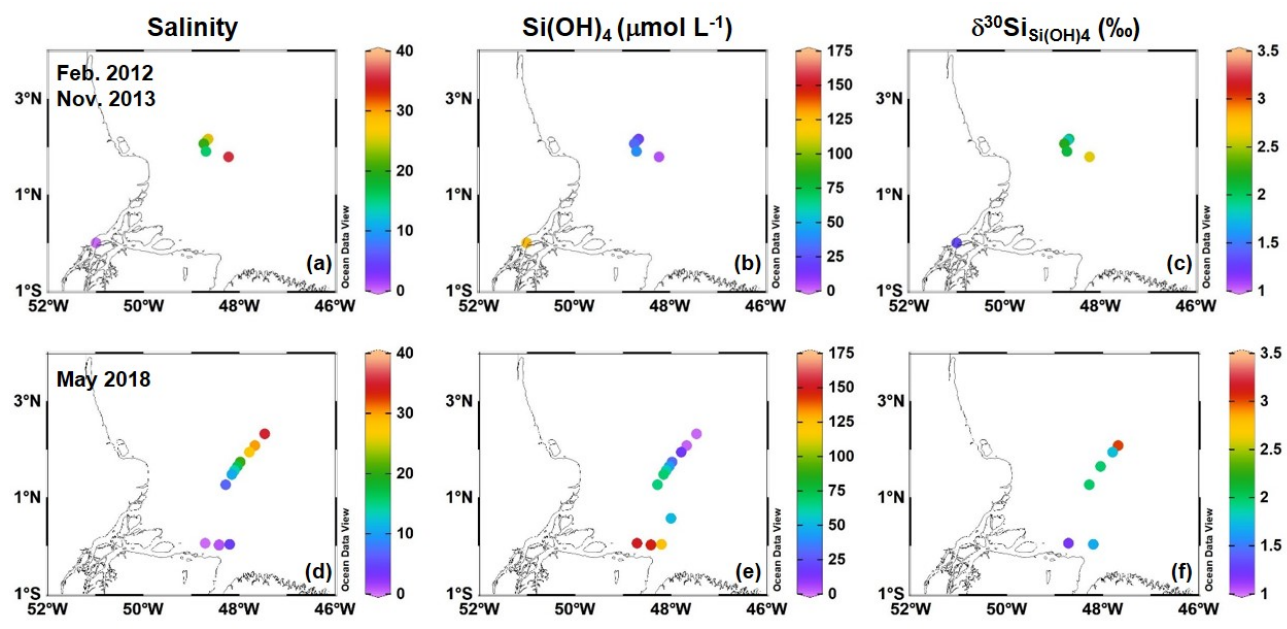
147 **Figure A1.** $\delta^{29}\text{Si}$ versus $\delta^{30}\text{Si}$ for the samples without brucite coprecipitation (red circles) and with
 148 brucite coprecipitation (blue triangles). All data points with error bars correspond to bracketing
 149 measurements ($\pm 2\text{SD}_{\text{bracketing}}$) in Tables 1 and A1. Least squares linear regression between $\delta^{29}\text{Si}$ and
 150 $\delta^{30}\text{Si}$ produces a slope of 0.5080 ± 0.0052 ($R^2=0.82$) for samples without brucite coprecipitation (red
 151 dashed line) and a slope of 0.5177 ± 0.0032 ($R^2=0.98$) for samples with brucite coprecipitation (blue
 152 dashed line). The theoretical kinetic fractionation line has a slope of 0.5092 for Si (grey dashed line)
 153 and the theoretical equilibrium fractionation line has a slope of 0.5178 for Si (black dashed line)
 154 (Grasse et al., 2017).



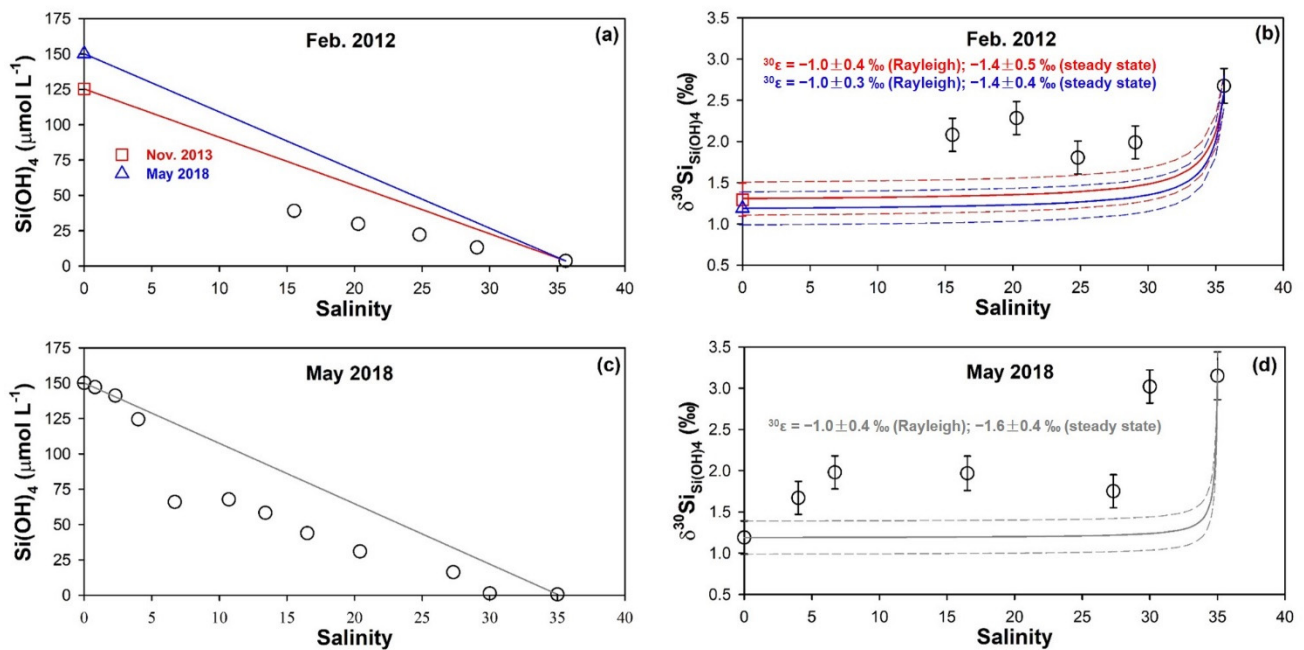
156 **Figure A2.** Bathymetric map showing the locations of sampling stations in the Amazon River Estuary
157 (November 2013) and the adjacent shelf area (February 2012).



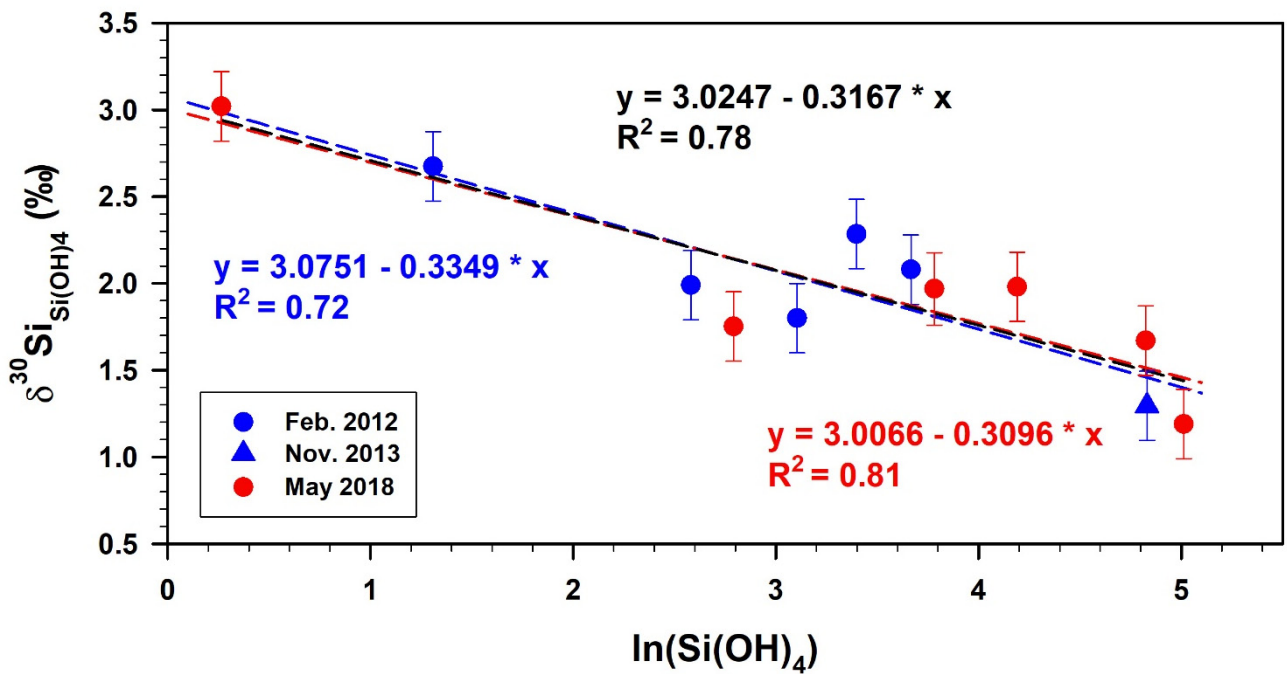
159 **Figure A3.** Surface distributions of salinity (a and d), dissolved silicate (Si(OH)_4 ; b and e), and
160 dissolved silicon isotopic compositions ($\delta^{30}\text{Si}_{\text{Si(OH)}_4}$; c and f) in the Amazon River Estuary and adjacent
161 shelf areas. Upper: November 2013 and February 2012; Below: May 2018.



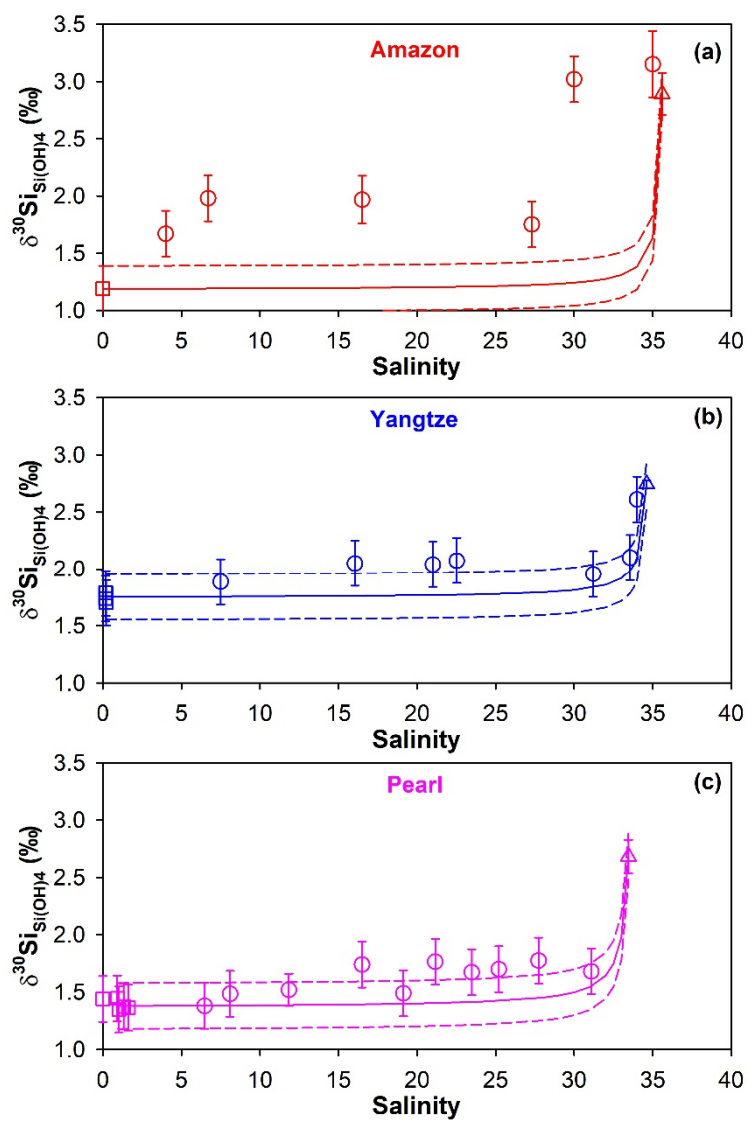
163 **Figure A4.** Dissolved silicate (Si(OH)_4) concentrations and dissolved silicon isotopic compositions
 164 ($\delta^{30}\text{Si}_{\text{Si(OH)}_4}$) distributions along salinity gradients in the Amazon River Estuary (black circles) in
 165 February 2012 (a and b) and May 2018 (c and d). The solid lines in each panel predict the conservative
 166 mixing for Si(OH)_4 or $\delta^{30}\text{Si}_{\text{Si(OH)}_4}$ between the river water and seawater endmembers, which are
 167 selected according to field measurements at the lowest and highest salinities. One exception is that the
 168 $\delta^{30}\text{Si}_{\text{Si(OH)}_4}$ value of seawater endmember in May 2018 (d) is estimated based on its Si(OH)_4
 169 concentration. In panels (a) and (b), the river water endmember is adopted from the measurements in
 170 November 2013 (red square) and May 2018 (blue triangle). In panels (b) and (d), the error bars of the
 171 field $\delta^{30}\text{Si}_{\text{Si(OH)}_4}$ data are the long-term external reproducibility of $\pm 0.20\text{‰}$ or the 2 standard deviations
 172 estimated from the repeated measurements if they are larger than $\pm 0.20\text{‰}$. The dashed lines above and
 173 below the corresponding solid line indicate errors deduced from the uncertainty in estimating the
 174 $\delta^{30}\text{Si}_{\text{Si(OH)}_4}$ endmember values.



176 **Figure A5.** Dissolved silicon isotopic compositions ($\delta^{30}\text{Si}_{\text{Si(OH)}_4}$) versus natural logarithm of silicate
 177 concentration ($\ln(\text{Si(OH)}_4)$) in the Amazon River Estuary in February 2012 (blue circles) and November
 178 2013 (blue triangle) and in May 2018 (red circles). The black dashed line shows the linear relationship
 179 based on all data: $\delta^{30}\text{Si}_{\text{Si(OH)}_4} = (3.02 \pm 0.19) - (0.32 \pm 0.05) \times \ln(\text{Si(OH)}_4)$ ($R^2 = 0.78$). The blue dashed line
 180 shows the linear relationship based on data collected in February 2012 and November 2013:
 181 $\delta^{30}\text{Si}_{\text{Si(OH)}_4} = (3.08 \pm 0.35) - (0.33 \pm 0.11) \times \ln(\text{Si(OH)}_4)$ ($R^2 = 0.72$). The red dashed line shows the linear
 182 relationship based on data collected in May 2018: $\delta^{30}\text{Si}_{\text{Si(OH)}_4} = (3.01 \pm 0.29) - (0.31 \pm 0.08) \times \ln(\text{Si(OH)}_4)$
 183 ($R^2 = 0.81$).



185 **Figure A6.** Dissolved silicon isotopic compositions ($\delta^{30}\text{Si}_{\text{Si}(\text{OH})_4}$) distributions along salinity gradients
186 in the Amazon (a), Yangtze (b) and Pearl (c) River estuaries. The solid lines in each panel predict the
187 conservative mixing for $\delta^{30}\text{Si}_{\text{Si}(\text{OH})_4}$ between the river water and seawater endmembers. While the river
188 water endmembers (squares) are selected according to field measurements at the lowest salinities (in
189 this study), the seawater endmembers (triangles) are selected from previous studies (de Souza et al.,
190 2012; Cao et al., 2012, 2015) as open ocean surface waters with nearly completely depleted $\text{Si}(\text{OH})_4$
191 and extremely heavy $\delta^{30}\text{Si}_{\text{Si}(\text{OH})_4}$. The error bars of the field $\delta^{30}\text{Si}_{\text{Si}(\text{OH})_4}$ data in each panel are the long-
192 term external reproducibility of $\pm 0.2\text{‰}$ or the 2 standard deviations estimated from the repeated
193 measurements if they are larger than $\pm 0.20\text{‰}$. The dashed lines above and below the corresponding
194 solid line indicate errors deduced from the uncertainty in estimating the $\delta^{30}\text{Si}_{\text{Si}(\text{OH})_4}$ endmember values.



References

- Cao Z., Frank M. and Dai M. (2015) Dissolved silicon isotopic compositions in the East China Sea: Water mass mixing vs. biological fractionation. *Limnol. Oceanogr.* **60**, 1619-1633.
- Cao Z., Frank M., Dai M., Grasse P. and Ehlert C. (2012) Silicon isotope constraints on sources and utilization of silicic acid in the northern South China Sea. *Geochim. Cosmochim. Acta* **97**, 88-104.
- De La Rocha C.L., Brzezinski M.A. and DeNiro M.J. (2000) A first look at the distribution of the stable isotopes of silicon in natural waters. *Geochim. Cosmochim. Acta* **64**, 2467-2477.
- de Souza G.F., Reynolds B.C., Rickli J., Frank M., Saito M.A., Gerringa L.J.A. and Bourdon B. (2012) Southern Ocean control of silicon stable isotope distribution in the deep Atlantic Ocean. *Global Biogeochem. Cycles* **26**, GB2035.
- DeMaster D.J., Smith W.O., Nelson D.M. and Aller J.Y. (1996) Biogeochemical processes in Amazon shelf waters: Chemical distributions and uptake rates of silicon, carbon and nitrogen. *Cont. Shelf Res.* **16**, 617-643.
- Ding T.P., Gao J.F., Tian S.H., Shi G.Y., Chen F., Wang C.Y., Luo X.R. and Han D. (2014) Chemical and Isotopic Characteristics of the Water and Suspended Particulate Materials in the Yangtze River and Their Geological and Environmental Implications. *Acta Geologica Sinica-English Edition* **88**, 276-360.
- Frings P.J., Clymans W., Fontorbe G., De La Rocha C.L. and Conley D.J. (2016) The continental Si cycle and its impact on the ocean Si isotope budget. *Chem. Geol.* **425**, 12-36.
- Georg R.B., Reynolds B.C., Frank M. and Halliday A.N. (2006) New sample preparation techniques for the determination of Si isotopic compositions using MC-ICPMS. *Chem. Geol.* **235**, 95-104.
- Grasse P., Brzezinski M.A., Cardinal D., de Souza G.F., Andersson P., Closset I., Cao Z., Dai M., Ehlert C., Estrade N., François R., Frank M., Jiang G., Jones J.L., Kooijman E., Liu Q., Lu D., Pahnke K., Ponzevera E., Schmitt M., Sun X., Sutton J.N., Thil F., Weis D., Wetzel F., Zhang A., Zhang

221 J. and Zhang Z. (2017) GEOTRACES inter-calibration of the stable silicon isotope composition
 222 of dissolved silicic acid in seawater. *J. Anal. At. Spectrom.* **32**, 562-578.

223 Hughes H.J., Bouillon S., André L. and Cardinal D. (2012) The effects of weathering variability and
 224 anthropogenic pressures upon silicon cycling in an intertropical watershed (Tana River, Kenya).
 225 *Chem. Geol.* **308-309**, 18-25.

226 Hughes H.J., Sondag F., Santos R.V., André L. and Cardinal D. (2013) The riverine silicon isotope
 227 composition of the Amazon Basin. *Geochim. Cosmochim. Acta* **121**, 637-651.

228 Mulitza S., Chiessi C.M., Cruz A.P.S., Frederichs T.W., Gomes J.G., Gurgel M.H.C., Haberkern J.,
 229 Huang E., Jovane L. and Kuhnert H. (2013) Response of Amazon sedimentation to
 230 deforestation, land use and climate variability - Cruise No. MSM20/3 - February 19 - March
 231 11, 2012 - Recife (Brazil) - Bridgetown (Barbados). In *MARIA S. MERIAN-Berichte*. DFG-
 232 Senatskommission für Ozeanographie, Bremen. **MSM20/3**.

233 Reynolds B., Frank M. and Halliday A. (2006) Silicon isotope fractionation during nutrient utilization
 234 in the North Pacific. *Earth. Planet. Sci. Lett.* **244**, 431-443.

235 Shipe R.F., Curtaz J., Subramaniam A., Carpenter E.J. and Capone D.G. (2006) Diatom biomass and
 236 productivity in oceanic and plume-influenced waters of the western tropical Atlantic ocean.
 237 *Deep Sea Res. Part I* **53**, 1320-1334.

238 Zhang J., Ren J.L., Liu S.M., Zhang Z.F., Wu Y., Xiong H. and Chen H.T. (2003) Dissolved aluminum
 239 and silica in the Changjiang (Yangtze River): Impact of weathering in subcontinental scale.
 240 *Global Biogeochem. Cycles* **17**, 1077.

241 Zhang S.R. and Lu X.X. (2008) Chemical and physical weathering in a mountainous tributary of the
 242 Zhujiang (Pearl River), China. In *Sediment Dynamics in Changing Environments* (eds. J.
 243 Schmidt, T. Cochrane, C. Phillips, S. Elliott, T. Davies and L. Basher). IAHS Publ., pp. 359-
 244 366.